Validation of an XCT/fDOT System on Mice

Author(s):
Koenig, Anne; Planat-Chrétien, Anne; Hassler, Kai; Bucher, Martina; Coutard, Jean-Guillaume; Hervé, Lionel; Brambilla, Marco; Josserand, Véronique; Coll, Jean-Luc; Vats, Divya; Dikaiou, Katerina; Rudin, Markus; Dinten, Jean-Marc

Publication date:
2012-04-12

Permanent link:
https://doi.org/10.3929/ethz-b-000059101

Originally published in:
ISRN optics 2012, https://doi.org/10.5402/2012/735231

International Scholarly Research Network
ISRN Optics
Volume 2012, Article ID 735231, 13 pages
doi:10.5402/2012/735231

Research Article

Validation of an XCT/fDOT System on Mice

Anne Koenig,[1] Anne Planat-Chrétien,[2] Kai Hassler,[3] Martina Bucher,[3] Jean-Guillaume Coutard,[2] Lionel Hervé,[2] Marco Brambilla,[2] Véronique Josserand,[4] Jean-Luc Coll,[4] Divya Vats,[5] Katerina Dikaiou,[5] Markus Rudin,[5] and Jean-Marc Dinten[2]

[1] *CEA, LETI, MINATEC, 17 Rue des Martyrs, 38054 Grenoble Cedex 9, France*
[2] *CEA, LETI, MINATEC, 17 rue des martyrs, 38054 Grenoble Cedex 9, France*
[3] *SCANCO Medical AG, Fabrikweg 2, 8306 Brüttisellen, Switzerland*
[4] *INSERM U823, Institut Albert Bonniot, 38706 La Tronche Cedex, France*
[5] *Institute for Biomedical Engineering, University and ETH Zurich, Wolfgang-Pauli-Strasse 10, 8093 Zürich, Switzerland*

Correspondence should be addressed to Anne Koenig, anne.koenig@cea.fr

Received 12 December 2011; Accepted 22 January 2012

Academic Editors: S. Liu and R. J. Zawadzki

In this paper we present systems for dual modality imaging, combining fluorescence-enhanced diffuse optical tomography and X-ray computed tomography. Fluorescence diffuse optical tomography is carried out in a cylindrical geometry, which ensures optimal sampling and a straight forward integration with the X-ray modality. Specific acquisition protocols and reconstruction software have been developed to this end. The X-ray computed tomography serves two purposes. First, it provides the anatomical information in the registered dual modality images. Second, it provides the actual shape and boundaries of the animal as a priori input to the fluorescence reconstruction algorithm. To evaluate the performance of the optical imaging system, experiments have been conducted on phantoms, mice with inserted fluorescing capillaries, and finally on mice bearing tumors, *ex-vivo* and *in-vivo*. Experiments on mice with capillaries inserted in different region of interest, allow estimating the detection limits of fluorophore concentrations. The fluorescence reconstructions are shown to be geometrically consistent with the X-ray images. Finally we demonstrate the capability of the bimodal system to localize real tumours in mice *in-vivo*. These results show that dual modality fluorescence-enhanced diffuse optical tomography and X-ray computed tomography imaging in cylindrical geometry has a high potential for small animal tumour evolution studies.

1. Introduction

Three-dimensional near-infrared fluorescence-enhanced Diffuse Optical Tomography (fDOT) has been proven to be an efficient noninvasive tool for preclinical cancer research [1, 2]. With it, the biodistribution of fluorescent probes targeting molecular markers of tumor development can be quantitatively estimated. Moreover, fDOT can be used to assess the influence of anti-cancer treatments on the molecular level, which makes it a relevant technique not only in fundamental research but also in drug development [3–5]. fDOT, as a molecular imaging modality analog to PET, does not readily provide anatomical information. However, structure can be obtained by combining fDOT with a second modality providing morphological information, such as MRI [6, 7], ultrasound [8, 9], or XCT [10–13]. In this way, obtaining *in vivo* anatomical and molecular information simultaneously becomes possible.

In the present work, XCT has been chosen as the second imaging modality because it provides high resolution, is relatively cheap, and its integration with optical tomography in a single instrument is straightforward. The dual-modality-approach facilitates the interpretation of the measured data as it allows the coregistration of molecular data with anatomical information. This way, the animal shape and boundaries from the XCT can be used as a priori input to the fDOT reconstruction algorithm.

The data presented in this paper were obtained on two instruments. The first one is a laboratory setup, which physically integrates the XCT and the fDOT modality. The second one is an industrial prototype, based on the technology tested on the laboratory setup. In contrast to the

laboratory setup, it features a horizontal rotation axis and the XCT and fDOT acquisition chains are physically separated. In both cases, fDOT scanning is performed in a cylindrical geometry. This approach allows sampling of a larger part of the animal surface as compared to a planar tomography setup. This results in superior imaging quality, as was shown previously [14, 15]. To provide high reconstruction accuracy, even in very heterogeneous tissue, the fDOT reconstruction algorithm takes optical heterogeneities into account [16].

In previous work, the laboratory system was characterized in terms of linearity, repeatability, detection limit, and resolution [14]. These studies were based on measurements taken on phantoms. In the present paper, measurements are presented that validate the systems and method on sacrificed mice and on mice *in vivo*. The fDOT reconstructions are evaluated in terms of the minimum fluorophore quantity required to overcome autofluorescence or nonspecific fluorescence, that is, injected fluorescence nontargeted to tumors, in the localization error of the reconstructed inclusions, and the presence of artefacts.

In the first part of this paper, we describe the optical imaging systems with details given about the instrumentation describing the two purposes of the XCT modality. First, it provides the actual shape and boundaries of the measured animal as *a priori* input to the fDOT reconstruction algorithm. Second, it provides anatomical information in the dual-modality images registered. The second part is devoted to the description of the method and algorithm used for the fDOT reconstruction. The third part presents results obtained on mice. In a first study, dead mice with a capillary containing fluorophore inserted in the trachea or in the abdomen were imaged on the laboratory setup. The results validate the registration between the XCT and fDOT images. In particular, the error in localizing the fluorescent inclusion was found to be smaller than 1 mm. This study also allowed determining the minimum fluorophore quantity necessary to overcome the signal due to natural or nonspecific fluorescence. Finally, experiments on mice bearing different types of tumors are presented. Two independent studies are discussed. The first one was conducted on the laboratory setup on dead mice bearing lung tumors. The second one was carried out on the industrial setup *in vivo* on live mice bearing subcutaneous tumors in the pelvic area.

2. Bimodal Instrumentation

2.1. Laboratory Setup. The cylindrical geometry is the most suitable geometry to deal with both modalities since XCT instruments are common in this geometry. Moreover, it allows a uniform scan of the entire object's surface, which favors the excellent performances of the system in terms of sensibility and isotropic resolution along all axes [15]. Previous studies have led to the development of a planar fDOT continuous wave (CW) tomograph [16–19]. To cope with this new geometry, we developed a cylindrical laboratory bench demonstrator as described on Figure 1.

The position of the illumination relative to the detection system, defining the optical axis, is fixed, mounted on an optical table. The optical axis is horizontal (in the x, y plane), and the observed animal is placed vertically on a rotation stage with a vertical rotation axis (around z), see Figure 2(a). Note that this geometry is dual from the one used on classical XCT systems where the source-detector pair is rotating. In order to scan vertically (along z) the examined object, the optical chain is mounted on synchronized translation stages and controlled by a computer.

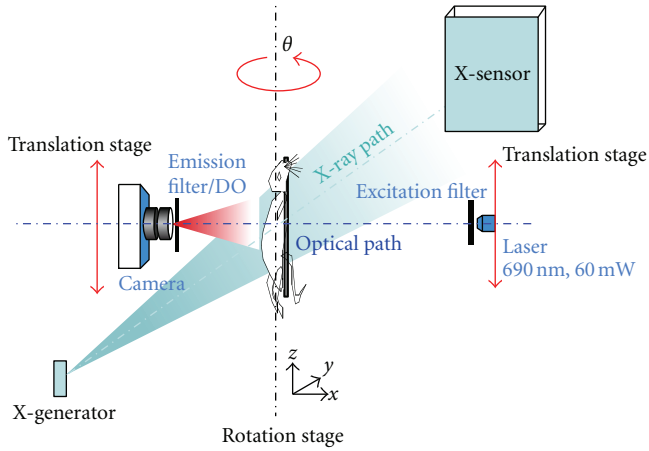

Figure 1: Schematic of the bimodal laboratory setup.

The XCT axis defined by the relative position of the X-ray detector and the X-ray generator has been placed perpendicular to the optical axis in the x, y plane. The optical chain bulk has been optimized according to X-ray constraints: geometric constraints, protection against radiation, against reflections. A geometrical calibration of the XCT and fDOT system by the use of a dedicated calibration object (cylindrical phantom with inserted reference balls that are visible both in XCT and fDOT modalities) is performed prior to acquisition and analysis of data.

The fDOT instrument chain consists of a continuous wave laser source (diode laser HEML, Frankfort Laser Compagny 685 nm, 60 mW), a high-sensitivity CCD camera (Andor DV438) and a combination of filters (coloured RG9, band-pass filter Semrock 775/46, and interference filter ALP 770) for fluorescence detection. The excitation and emission wavelengths of the system and the fluorophores are chosen in the visible range, close to NIR, that is, the so-called therapeutic window to optimize transmission through the whole animal. A custom-made, easy to use holder presented in Figures 2(b)–2(d) has been designed for use with both modalities, that ensures the animal is immobile and in an almost "natural" position even though it is vertical.

2.2. Industrial Prototype. Based on the fDOT system described above, an fDOT industrial prototype scanner (see Figure 3(a)) was developed at SCANCO Medical after industrial transfer of the technology [20]. This scanner features a 360° projection, transillumination geometry, just as the lab-setup described in Section 2.1. However, the rotation axis is horizontal, which allows a more natural position of the animal and easier anesthesia setup. The change in

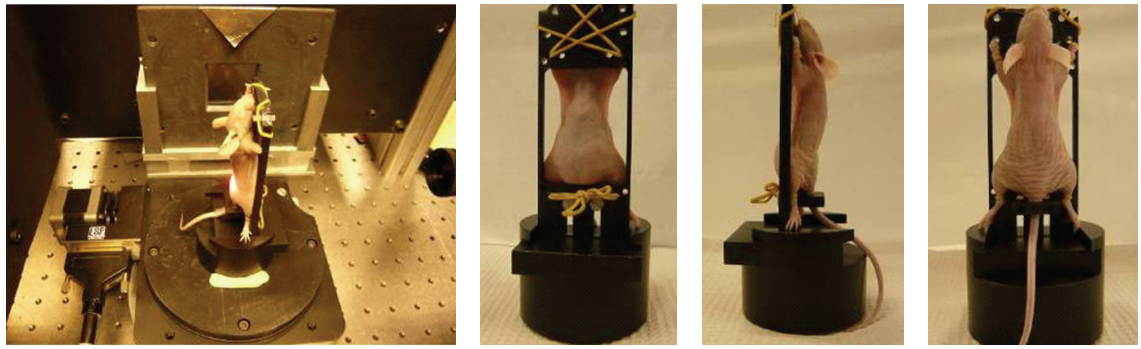

(a) (b) (c) (d)

Figure 2: Photograph of the bimodal laboratory setup (a) and of a mouse in the holder (b, c, and d).

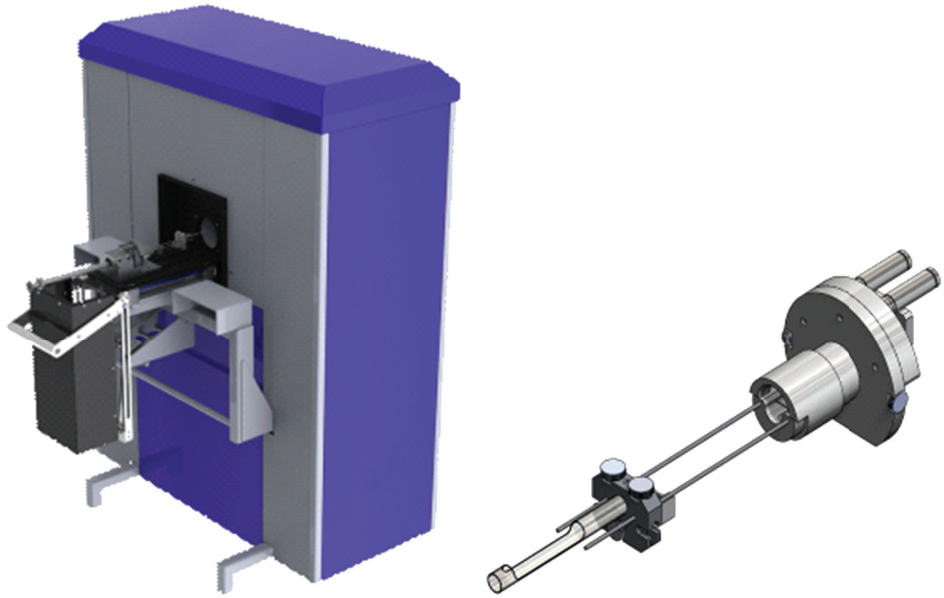

(a) (b)

Figure 3: Illustration of the prototype fDOT scanner (a). A dedicated animal-holder is used to move the animal between different scanners to achieve multimodality imaging (b).

scanning-geometry is achieved by mounting the illumination system and the detection system on a platform that can be rotated around the animal. The animal is placed on a holder that can be translated along the rotation axis of the platform, which allows for uniform sampling of the animal surface in two directions. An additional advantage of the horizontal scanning geometry is its increased compatibility with other imaging technologies. Because the described geometry is the preferred one in many existing small animal imaging systems, moving the animal between systems and thus registering of images from different modalities is simplified. The scanner features two diode lasers emitting at 650 nm and 690 nm. A fiber switch allows selection of the excitation wavelength. Fluorescence emission bands are selected by means of a filter changer comprising interference filters optimized for Alexa Fluor 680 and Alexa Fluor 750. Transmission measurements at the excitation wavelength are performed with an ND filter (OD 2.25) in the detection path. The whole illumination and detection system is enclosed by a lightproof housing that allows measurements to be taken under typical workplace lighting conditions.

While the first lab setup integrates the microCT and an fDOT system on a single measurement platform, the present scanner does not yet. MicroCT measurements are performed on a separate system (vivaCT, SCANCO Medical AG, Switzerland). The link between the two modalities is provided by a dedicated animal holder that can be moved from one system to the other (Figure 3(b)). This holder is fixed to an adapter on either of the two scanners in a precise and repeatable manner. As a result, the position of the animal inside the fDOT system can be determined by a microCT scan, provided an appropriate geometrical calibration has been performed once. The geometrical calibration is achieved prior to the measurements, in a similar manner

as it is done for the laboratory system, that is to say by means of a calibration object, which is visible in both, the XCT and fDOT modalities. The transformation matrix that relates the coordinate systems to each other is calculated automatically from the optical and the microCT images by software developed by the authors.

3. Method

3.1. Effective Coupling of XCT/fDOT. The effective coupling of XCT/fDOT modalities occurs at different levels of the process. First, the XCT image is used as *a priori* information for the fDOT algorithm (external shape of the mouse); second, it gives anatomical information to help with fDOT image interpretation.

The X-ray acquisition protocol defines the number of acquired projections and the voltage, current, and filtering of the X-ray generator. The reconstruction of the volume of interest is then conducted using, for example, the classical Feldkamp algorithm [21].

The optical acquisition protocol defines the reference, diffusion, and fluorescence data acquired according to a set of angular positions and Z-positions. A dark noise and optical vignetting effects correction is performed as preprocessing of the data before they are used in the fDOT algorithm for reconstruction.

(i) Reference data are acquired on a reference object (with known optical coefficients) at the excitation wavelength, for each source-camera position to calibrate the system for quantification purpose [22]. This calibration is done once, prior to each series of experiments.

(ii) Diffusion and fluorescence data are acquired on the object to be reconstructed at both excitation and emission wavelengths, for each source-camera position.

The method used in the system is described in six Steps in Figure 4 using the example of a phantom mimicking the mouse shape and with similar optical properties ($\mu_a = 0.24\,\mathrm{cm}^{-1}$, $\mu_s' = 10\,\mathrm{cm}^{-1}$). A solid fluorescent inclusion ($1\,\mathrm{mm}^3$) visible in XCT modality has been inserted in it. After positioning the object or the animal on the bench (Step 1) and acquisition and reconstruction of XCT data according to the X-ray acquisition protocol (Step 2), the external shape of the object is extracted from the XCT volume (Step 3). The XCT reconstructed volume is then discretized to form a mesh (finite volumes) and used by the fDOT algorithm to solve the light propagation equation taking into account actual object boundaries. Figure 5 shows the surface extracted from the XCT volume (color) superimposed on the XCT image (grey level) for a mouse imaged on the lab setup.

The laser source is approximated thanks to the diffusion approximation by an isotropic point source—called excitation point source—located inside the object at $1/\mu_s'$ from the boundary. For each of the "detector-source" positions defined in the optical acquisition protocol, the intersection of the excitation light beam with the object's surface is determined. The intersection point is calculated with a ray-driven method ((a) in Figure 6). This method calculates the intersection point of the light ray from the excitation source with the object's surface. In the case of an object with a complex shape, several intersection points may be found for a single light ray. Hence, the algorithm has to be capable of selecting the relevant intersection point. The nearest point to the laser source is selected (entering point) ((b) in Figure 6). The same approach is used to calculate the projections of the detectors onto the object's surface. We finally obtain the geometry used in fDOT reconstruction described in (c) in Figure 6, with the mesh displayed as black dots. The excitation point sources obtained with the ray-driven method described above are represented as red dots and the detector positions are shown in blue.

The laser scanning and image acquisition is performed according to the optical acquisition protocol as illustrated on Figure 4 Step 4. The 3D reconstruction of the fluorescence yield is then achieved (Step 5) by using the method developed in our laboratory [23] and described in the next section. Finally, visualization and quantification of the fluorescence is performed on a merged volume of both modality images (Step 6).

3.2. Reconstruction Method. This method allows the reconstruction of fluorescence even in highly attenuating media such as the liver or lungs. A map of optical heterogeneities is reconstructed first from diffusion data. It compounds the intrinsic tissue heterogeneity and the border effects due to the complex shape of the turbid medium. Then fluorescence is reconstructed from fluorescence data. In this study, the propagation of light modeled as a scalar field $\phi(\mathbf{r})$ in highly diffusive media (with $\mathbf{r}$ position in the studied medium belonging to a domain Ω with boundary $\mathrm{d}\Omega$) is assumed to follow the diffusion approximation equation:

$$-\nabla D(\mathbf{r})\nabla\Phi(\mathbf{r}) + \mu_a(\mathbf{r})\Phi(\mathbf{r}) = q_0(\mathbf{r}) \quad (\text{in}\,\Omega), \tag{1}$$

where $q_0(\mathbf{r})$ is the source term and $D(\mathbf{r}) = [3\mu_a(\mathbf{r})(\mu_a(\mathbf{r}) + \mu_s'(\mathbf{r}))]^{-1}$ is the diffusion coefficient, $\mu_a(\mathbf{r})$ is the absorption coefficient and $\mu_s'(\mathbf{r})$ is the reduced diffusion coefficient. A simplification of (1) leads to the simplified Helmotz equation as explained in [24]

$$\begin{aligned} &-\nabla^2\psi + \eta\psi = \frac{q_0\delta(\mathbf{r}-\mathbf{r}_s)}{\sqrt{D(\mathbf{r}_s)}} \\ &\text{with}\,\eta = \frac{\nabla^2\sqrt{D(\mathbf{r})}}{\sqrt{D(\mathbf{r})}} + \frac{\mu_a(\mathbf{r})}{D(\mathbf{r})},\ \psi = \sqrt{D}\phi, \end{aligned} \tag{2}$$

δ is the Dirac function to modelize a source positioned at $1/\mu_s'(\mathbf{r})$ inside the medium. $\eta(\mathbf{r})$ is a scalar map we call the "heterogeneities map," which compounds the attenuation and reduced scattering coefficients, and can also take into account effects of diffusion variations. The Helmotz equation (2) has a solution given by the Green function G and leads to(3)

$$\psi = \frac{q_0}{\sqrt{D(\mathbf{r}_s)}} G(\mathbf{r}_s, \mathbf{r}). \tag{3}$$

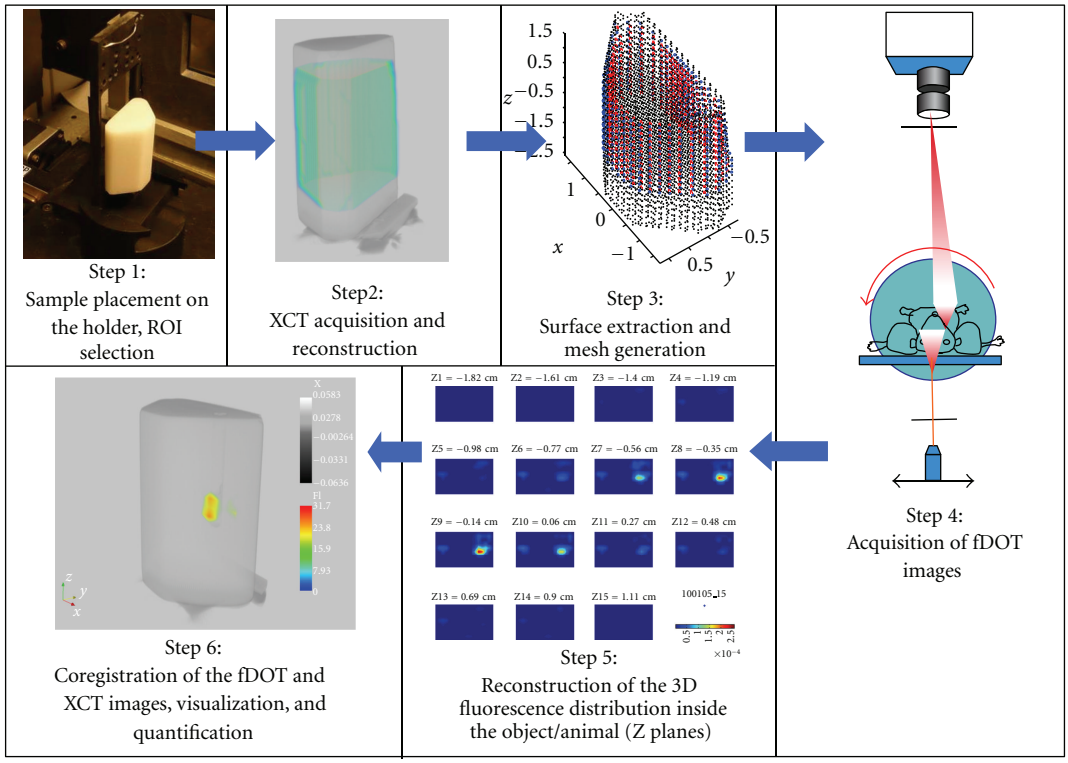

Figure 4: Illustration of the system method in six Steps, ROI (region of interest) selection, XCT reconstruction, surface extraction, and mesh generation, fDOT image acquisition, fDOT reconstruction, coregistration vizualisation, and quantification of fDOT and XCT images.

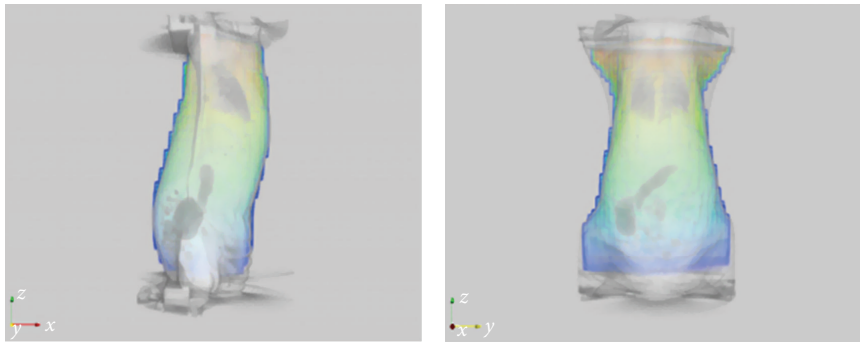

(a) (b)

Figure 5: XCT reconstructed volume (grey level) and surface extracted from XCT volume used in fDOT reconstruction superimposed (color).

So, given an η map, we can compute the propagation function $G(\mathbf{r}_1, \mathbf{r}_2)$ of light in the medium between any points $\mathbf{r}_1$ and $\mathbf{r}_2$:

$$(\nabla^2 - \eta)G(\mathbf{r_1}, \mathbf{r_2}) = -\delta(\mathbf{r_1} - \mathbf{r_2}). \quad (4)$$

By modelling the laser source s as a Dirac delta function position at $\mathbf{r_s}$, (1) and (4) give the excitation density wave $\Phi^x(\mathbf{r})$ at any point $\mathbf{r}$ of the medium:

$$\Phi^x(\mathbf{r_s}, \mathbf{r}) = \lambda G(\mathbf{r_s}, \mathbf{r}). \quad (5)$$

λ is a conversion factor related to the laser source intensity and the detection efficiency of the camera and is determined by calibration on the reference acquisition data. It is such also dependant on the diffusion of the reference phantom D_0

A discrete version of (4) is solved on the mesh extracted from the X-CT volume. Using its external shape, we complete the equation system with the "Robin conditions" [25], see (6), where $\mathbf{\Phi}_{\text{bnd}}(\mathbf{r})$ stands for the field at the boundary and $\vec{n}(\mathbf{r})$ for the outward normal vector:

$$\Phi_{\text{bnd}}(\mathbf{r}) + \alpha D \nabla \Phi_{\text{bnd}} \cdot \vec{n}(\mathbf{r}) = 0. \quad (6)$$

The global reconstruction process is then performed in two main Steps. We first compute the heterogeneities

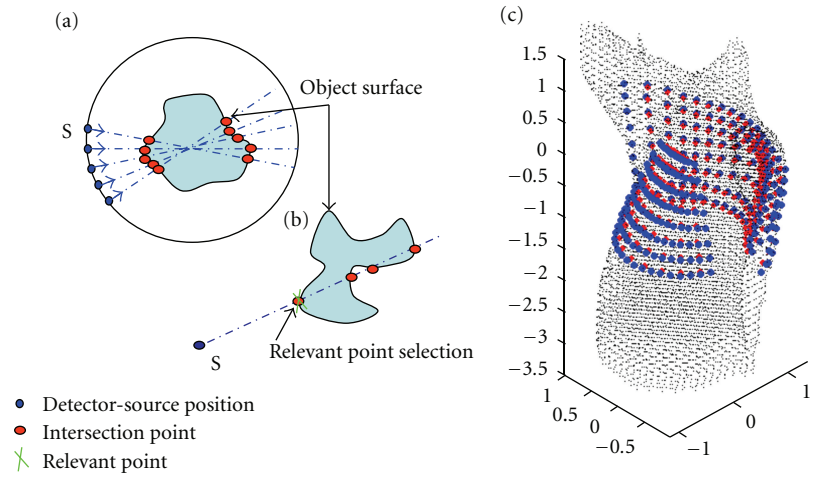

Figure 6: Using the external shape derived from the XCT volume to define the excitation source points. (a) Illustration of the ray-driven approach. (b) Selection of the relevant excitation source intersection point for complex shapes. (c) Mesh obtained for a mouse, used for fDOT reconstruction. The nodes of the mesh are displayed as black dots. Sources (red dots) are located at 24 azimuth angles and 12 longitudinal positions. The intensity of fluorescence and excitation light is sampled at the detector positions shown in blue.

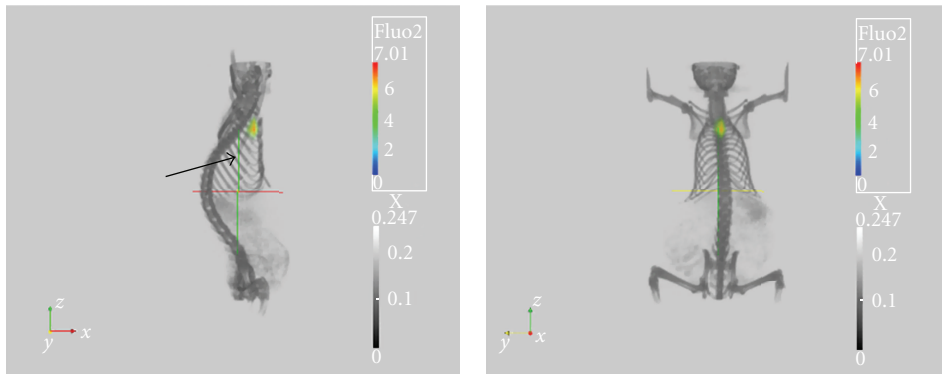

Figure 7: Mouse no. 1: mouse with capillary tube with 5 pmol of Alexa 750 inserted in the lungs area; coregistration of the fDOT and XCT images (visualization threshold 50%).

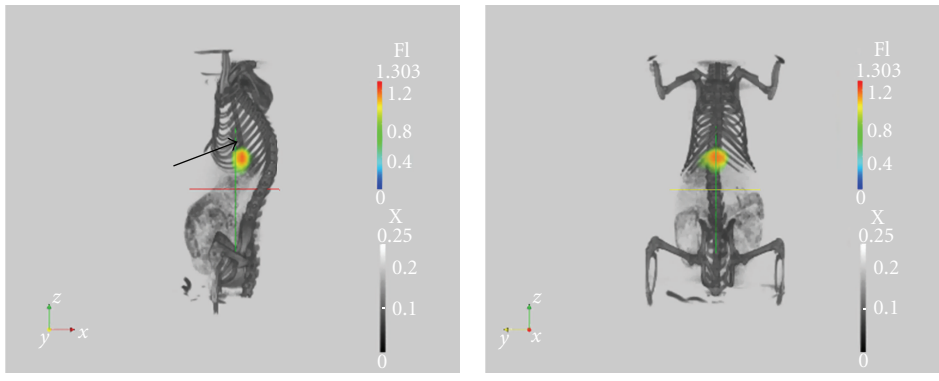

Figure 8: Mouse no. 2: mouse with 2 pmol Alexa 750 inside a capillary tube—visible also in XCT modality on (a) (arrow)—inserted in the lungs. Coregistration of the fDOT and XCT images (visualization threshold 50%).

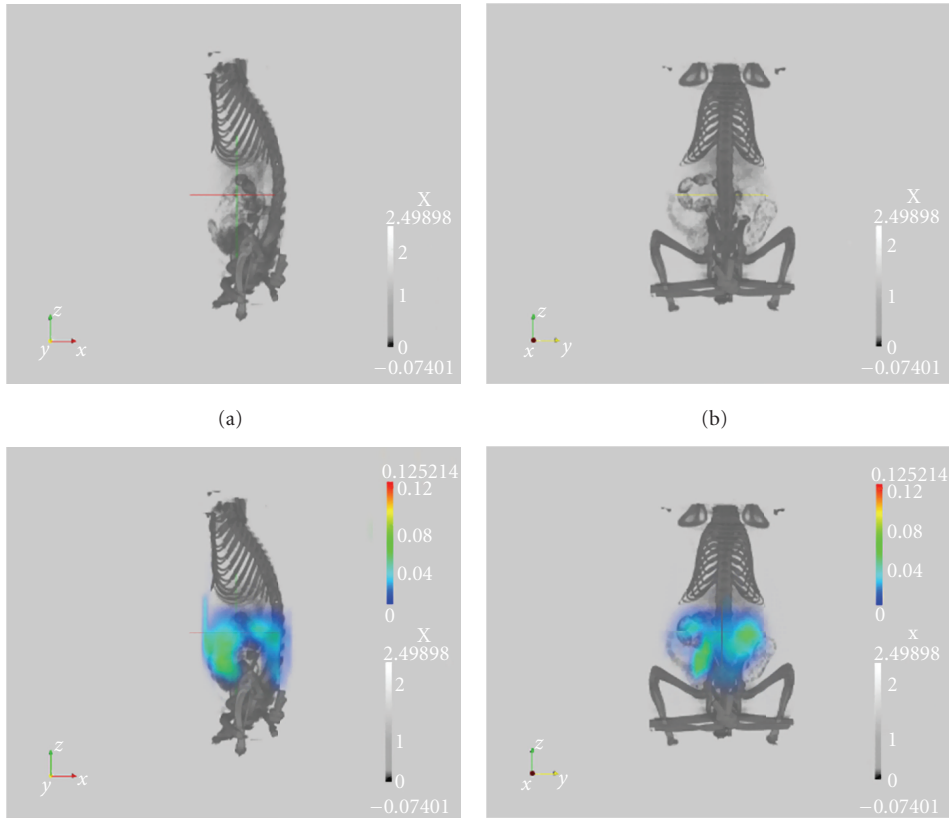

Figure 9: Mouse no. 3, experiment on abdominal area. (a, b) XCT reconstruction only, the heterogeneous aspect of the abdomen is clearly visible. (c, d) coregistration of the fDOT and XCT images for the mouse, with 5 pmol Alexa 750 inside a capillary tube inserted in the abdominal area. It is impossible to distinguish specific fluorescence from autofluorescence.

$\eta(\mathbf{r})$ map by comparison of the Green's functions (light propagating between the source s and the detector d) $G(\mathbf{r_s}, \mathbf{r_d})$ to the excitation measurements. This first Step ("Heterogeneities" method) is itself an iterative process initialized with a homogeneous map $\eta_0(\mathbf{r})$. The second Step is the reconstruction of the fluorescence yield from fluorescent measurements using the heterogeneity map obtained with the diffusion data, as explained in [22].

As said before, $\Phi^x(\mathbf{r})$ denoted the excited light absorbed by the fluorophore at point $\mathbf{r}$, so the emitted light equals to $S_f(\mathbf{r}) = \Phi^x(\mathbf{r})X(\mathbf{r})$ with $X(\mathbf{r})$ proportional to the fluorophore concentration in $\mathbf{r}$. The detected signal in detector d is given in $\mathbf{r}_d$. by

$$\Phi^m(\mathbf{r}_d) = q_0 \int \frac{G(\mathbf{r}_s, \mathbf{r})}{\sqrt{D(\mathbf{r}_s)}} \frac{X(\mathbf{r})}{D(\mathbf{r})} \frac{G(\mathbf{r}, \mathbf{r}_d)}{\sqrt{D(\mathbf{r}_d)}} d\mathbf{r}. \quad (7)$$

Note that we assume that the medium optical properties remain constant at the excitation and emission wavelength. Thus we reconstruct the quantity $X(\mathbf{r})/D(\mathbf{r})$, that is, the fluorescence concentration divided by the local diffusion coefficient $D(\mathbf{r})$. As demonstrated in [24], unless $D(\mathbf{r})$ is known, there is no unique solution to the fluorescence yield reconstruction.

Convergence of the fluorescence reconstruction algorithm is achieved within 15 iterations by using a classical iterative ART algorithm with a relaxation parameter of 0.1. We have shown on different mice experiments that further iterations with this relaxation factor induce nonsignificant variations of the ||measures − reprojections|| norm.

4. Measurements and Results

This section presents different kinds of experiments conducted on mice. First experiments were done to determine the minimum fluorophore quantity required to overcome of natural or nonspecific fluorescence. These experiments were conducted on the laboratory setup on sacrificed mice in which capillaries were inserted (mice no. 1 to no. 4). Afterwards, experiments were done on the laboratory setup to validate the feasibility of imaging tumor-bearing mice (mice from no. 5 to no. 7). As no anaesthetic system is installed on the laboratory setup, the mice were sacrificed just before measuring with the laboratory setup. Finally, *in vivo* experiments were conducted on the industrial setup (mice from no. 8 to no. 10).

Mice used on the laboratory setup were on a chlorophyll-free diet before the measurements were performed, whereas

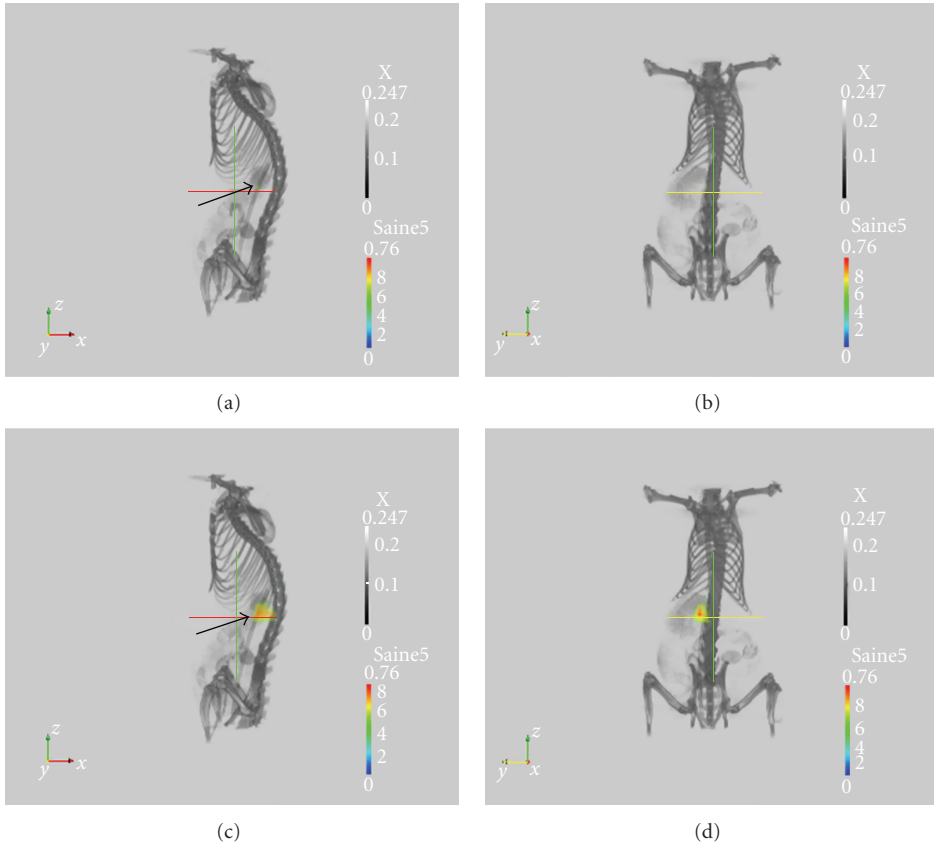

Figure 10: Mouse no. 4, experiment on abdominal area. (a, b) XCT reconstruction only, the heterogeneous aspect of the abdomen is clearly visible. (c, d) coregistration of the fDOT and XCT reconstructions for a mouse with 10 pmol Alexa 750 inside a capillary tube (arrow) inserted in the abdominal area. It is possible to distinguish specific fluorescence from natural fluorescence.

mice used on the industrial setup were not. All the animals used in this study were treated and handled according to the animal experimentation ethical committee Cometh38 for the laboratory setup and in strict adherence to the Swiss Law for Animal Protection for the industrial setup.

4.1. Measurements on Dead Mice Containing a Fluorescent Inclusion. Four experiments were conducted on mice either on the thorax or on the abdominal area. A capillary tube—filled with a solution of Alexa 750—was inserted either in the lungs via the trachea or in the abdomen of sacrificed healthy nude mice. In order to determine the concentration of fluorophore required to overcome natural or nonspecific fluorescence for each region of interest, we compare the fDOT reconstruction to the reconstruction of the same experiment with the mice imaged without the capillaries inside.

The X-ray generator is a monoblock X-ray source, manufactured by Gilardoni (Italy) with a CW power of 500 W. The anodic voltage is tunable from 40 kV to 140 kV allowing X-ray emission with an energy spectrum spreading from about 5 keV to 140 keV. The flux of the radiation emitted by the tungsten anode is controlled by the electrode current intensity adjustable from 1 mA to 7 mA. In our case, X-ray data are acquired according to a fast protocol with 400 projections at 40 kV, 6 mA, and a 50 μm Tin filtering. The Focal spot is approximately 1 mm. The X-ray detector is from Hamamatsu, Japan: C7942-CA with a 1 mm aluminium window. A preliminary Step of 4× binning (560×592 pixels^2 images) reduces the size of the acquired data and is sufficient for providing external shape information for fDOT. The reconstructed volume consists of $300 \times 300 \times 420$ voxels @ $150 \times 150 \times 150\,\mu$m^3 (x, y, z).

fDOT data are acquired according to 40×12 sources positions (12 vertical translations and 40 rotations). A rectangular detection area is selected onto the camera images according to the projection of the field of view and binned to form a grid of 40×12 detectors. Some views are removed to avoid the artefacts induced by the mouse holder (i.e., the views for which the optical axis intersects the mouse holder). The total reconstructed volume is composed of $17 \times 13 \times 26$ voxels of $2 \times 2 \times 2$ mm^3; the integration time was 3 s per frame for fluorescence images and 400 ms per frame for diffusion images.

On the laboratory setup, not optimized for acquisition times, the total X-ray acquisition takes about 5 minutes, the DOT acquisition 20 minutes, and the fDOT acquisition 40 minutes, so about 1 hour total acquisition time per mouse. The reconstruction time for XCT is about 10 minutes and 10 minutes for fDOT on a 2.6 Ghz PC (pentium 4).

The coregistered fDOT and XCT images are presented on Figures 7(a) and 7(b) (two view angles) for the lungs area experiment on mouse no. 1. The capillary is filled with 2.5 μL of Alexa 750 at a concentration of 2 μmol/L; that is, with a 5 pmol quantity. The results in Figure 7 highlight clearly the position of the capillary tube visible also in XCT modality on the left image (arrow). We localized the fluorophore in the morphology of the animal with a tolerance of 1 mm.

This experiment was repeated with a quantity of 2 pmol in the capillary Figure 8. This was the minimal quantity necessary to overcome the natural fluorescence in this area. We localized the fluorophore in the morphology of the animal with a tolerance of 1 mm.

The result for the abdominal area experiment on mouse no. 3 is presented on Figure 9. The capillary was filled with a quantity of 5 pmol as for experiment on mouse no. 1. The autofluorescence in the abdomen is much higher than in the lungs, despite the chlorophyll-free diet. Therefore, it was impossible to distinguish specific fluorescence from autofluorescence. For this reason, we performed the same kind of study with a fourth mouse filling the capillary with 2.5 μL of Alexa 750 at a concentration of 4 μmol/L; that is, with a quantity of 10 pmol. The result for the abdominal area experiment on mouse no. 4 is presented in Figure 10. It is now possible to distinguish specific fluorescence from natural fluorescence; the result is comparable to experiment on mouse no. 1 on lungs.

In this first series of experiments, we determined the minimal detectable fluorophore quantities for different areas of the mouse. Specifically, we found the minimum quantity for the lungs to be 2 pmol and for the abdomen 10 pmol. This difference is both due to the different absorption properties of the two types of tissue (absorbent region for the lungs and very heterogeneous region presenting intrinsic fluorescence for the abdomen), but also due to the different levels of autofluorescence present. Although we found a sensitivity limit of 2 pmol for the lungs, we now routinely use 5 pmol to ensure detection of capillary tubes despite variable absorption across different mice and depending on the position of the tube (more difficult when positioned near the liver).

For each one of these experiments, the use of the bimodal system leads to accurate results in terms of localisation with a tolerance of 1 mm depending of the size of the mesh (here 2 mm), independent of the zone of interest. It opens the field for further experiments of diseased mice and registration of fluorescence sources (targeted tumors) in the anatomy of the mouse.

4.2. Measurements on Tumor-Bearing Dead Mice. For tumor bearing mice, we define the optical acquisition protocol with 28×6 sources positions (6 vertical translations and 28 rotations, that is, we suppress views of the mouse holder at the acquisition Step) and the reconstructed volume with $29 \times 32 \times 48$ voxels of $1 \times 1 \times 1$ mm^3 to have a better resolution, the integration time was adapted according to the position.

We used CreLox inducible$p53-/-rb-/-$ transgenic mice. Adenovirus encoding Cre Recombinase is administered intratracheally, which induces lung tumor formation in 192 ± 36 days. We image the mice 244 days after infection: for that 10 nmol of Angiolone (Fluoptics) marked with AlexaFluor 700 (Invitrogen) were injected intravenously 4 h before imaging. It has been shown that this probe targets the $\alpha_v\beta_3$ integrin, which is overexpressed in tumors.

The fluorophore quantity is far higher than that used for capillaries inserted into the mouse. This is calculated based on the fact that in the animal, 1% of the injected dose is targeted per gram of tumor, that is, 100 pmol/g tumor. Moreover, highly diseased lungs weigh around 1 g so the maximum quantity for any tumor is 1 g.

We show in Figure 11 the results from two mice; the distribution obtained (small distinct tumoral sites in mouse no. 5 and a unique large site in mouse no. 6) was confirmed by the subsequent autopsy. As these tumours are not visible in XCT, only qualitative localization accuracy can be concluded. The fluorescence level has been quantified by FRI on the lungs after excision and confirms the reconstruction results. To verify that the fluorescence observed was specific, a control healthy mouse, mouse no. 7, was measured and the results are presented in Figure 12 on the same scale as Figure 11. The detected fluorescence is far lower than for tumour-bearing mice no. 5 and no. 6.

4.3. In Vivo Measurements on Tumor-Bearing Mice. Three *in vivo* measurements were conducted on nude mice bearing tumor xenografts using the industrial prototype. C51 tumor cells were implanted subcutaneously close to the base of the spine or at the thigh, ten days prior to measuring. Two of the mice were injected with two doses of 1 nmol Prosense 680 (VisEn Medical) via the tail vein. Prosense 680 is a probe that is activated by proteases and in particular by cathepsin, which is overexpressed in the tumor cells used here. The first dose of 1 nmol was injected approximately 48 hours and the second 24 hours before imaging. The third mouse served as a control and did not receive any injection of contrast agent. Before performing the fDOT measurements, food was withdrawn for four hours.

fDOT measurements were performed at an excitation wavelength of 650 nm. The power applied was about 1 mW at all source positions and the integration time was 200 ms per frame.

We performed microCT measurements on a vivaCT (SCANCO Medical) immediately after the fDOT measurements. The images obtained were segmented and used to generate the mesh for fDOT reconstruction (see (c) in Figure 6), as described above in Section 3.1. After reconstruction, the images obtained with the two modalities were segmented and registered.

Figure 13 to Figure 15 show views of the registered microCT and fDOT data obtained from the three *in vivo* experiments. Postprocessing of the microCT images was performed to visualize bone and skin. In all three cases the tumor masses form ulcers that are readily discernable on the microCT images. The reconstructed fluorophore distributions are visualized as iso-surfaces, showing the concentration at 50% of the reconstructed maxima. In all three cases, some fluorescence is reconstructed that is not readily attributable to the tumor tissue. Nonspecific

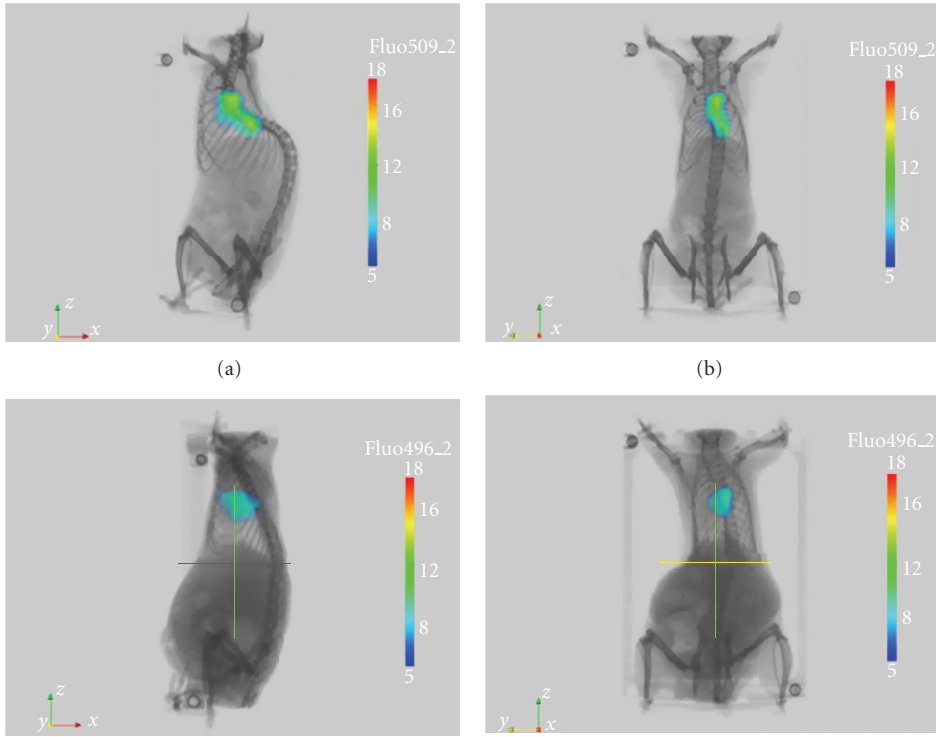

Figure 11: Experiment on tumour-bearing mice, small distinct tumoral sites in the lungs of mouse no. 5 (a, b), and a unique large sites in the lungs of mouse no. 6 (c, d).

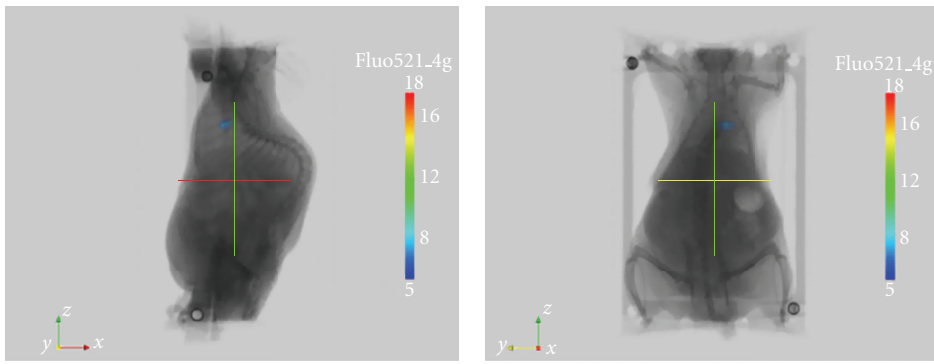

Figure 12: Experiment on healthy control mouse no. 7, with the same experimental protocol in Figure 11 for mice no. 5 and no. 6.

fluorescence was reconstructed in the abdomen and might stem from fluorescent substances found in food, as those animals were not placed in a chlorophyrle-free diet, also due to autofluorescence or nonspecific fluorescence (i.e., fluorescence not targeted to tumors).

Mouse no. 8 bears one tumor (arrow) close to the spine (Figure 13), which is clearly visible in both microCT and fDOT modalities. Here, the maximum reconstructed fluorophore concentration is about six times above the maximum detected for the control case no. 10 (Figure 15). This mouse had a second, smaller tumor close to its left knee. An ulcer is visible in the microCT image but is not detected by the fDOT modality. The location of the second tumor made the measurements more challenging, as most of the source and detector positions are at a relatively far distance from the tumor site. Tissue at this specific location is not optimally sampled, which might lead to a decreased detection sensitivity at this particular location.

In mouse no. 9 (Figure 14) grew one, large tumor at the left thigh (arrow). The tumor is clearly reconstructed by the fDOT algorithm as a torus-like shape. Some nonspecific fluorescence was reconstructed in the abdomen.

Figure 15 shows the distribution of fluorophore for the control case, which is a noninjected diseased mouse (mouse

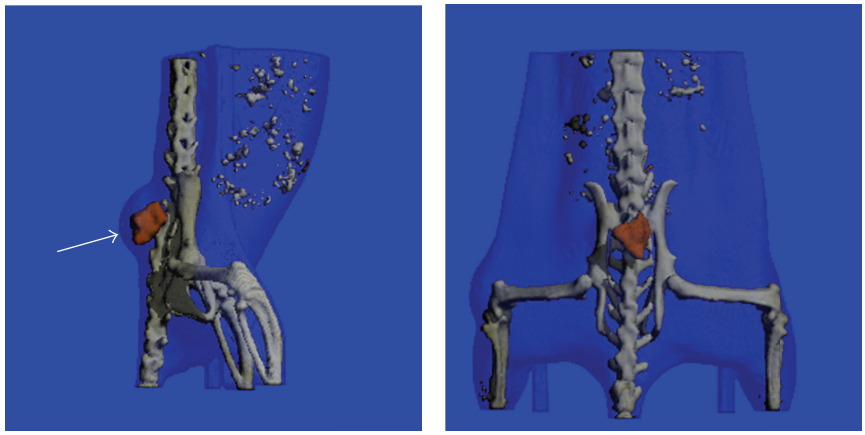

(a) (b)

Figure 13: Two views of the coregistered data obtained for mouse no. 8. The biodistribution of the protease targeting probe as obtained by the fDOT measurement is shown in red. The threshold applied for visualization of the fluorophore distribution is 50% of the reconstructed maximum. Skin is shown in transparent blue and bones are shown in grey.

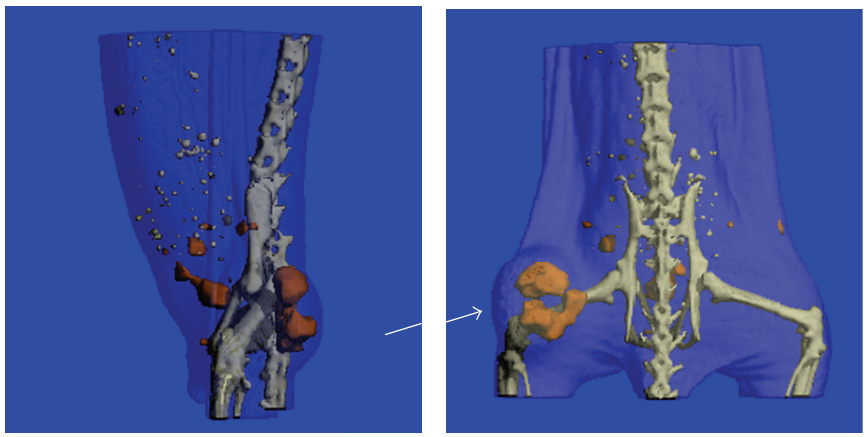

(a) (b)

Figure 14: Two views of the coregistered data obtained on mouse no. 9. The visualization of the data is realized as described in Figure 13.

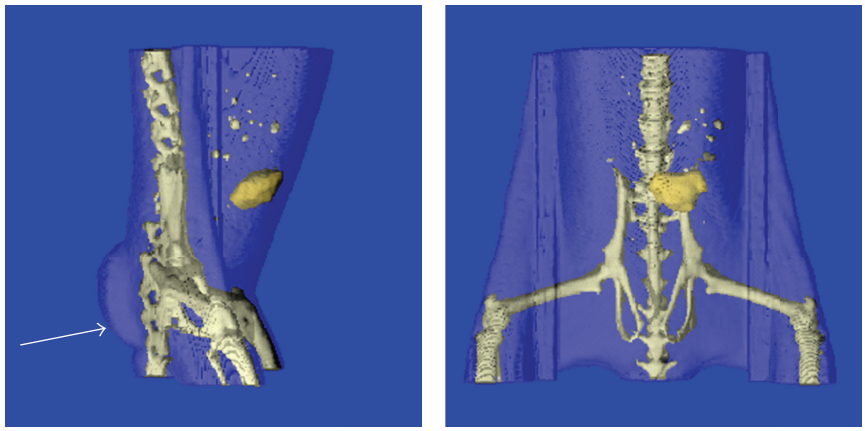

(a) (b)

Figure 15: Two views of the coregistered data obtained on mouse no. 10 (control, bearing a tumor but no protease-targeting probe was injected). Reconstructed auto-fluorescence is shown in yellow. No fluorescence is reconstructed at the tumor site, which forms an easily discernable ulcer close to the lower part of the spine ((b), arrow).

no. 10). No fluorescence activity was detected in the tumor tissue (the ulcer is visible close to the lower spine, arrow), but some fluorescence was located in the lower abdomen. However, the reconstructed maximum concentration is at least a factor of 2 below the threshold applied in the two cases discussed above.

5. Conclusion

Two systems, a laboratory setup and an industrial prototype, dedicated to the multimodal optical and X-ray measurements, have been developed. Experiments have been successfully conducted on sacrificed mice with a capillary tube containing Alexa750, inserted either in the trachea or the abdomen. We have thus determined the limit of sensitivity of the laboratory system to detect fluorescence signal over natural or nonspecific fluorescence. For lung area, this limit is 5 pmol; for the abdomen it is 10 pmol. The fluorophore localization is in accordance with the X-ray reconstruction. Some experiments on mice bearing tumors showed that the reconstructed fluorescence in the case of mice without tumors is far lower than the quantity reconstructed for mice bearing tumors. In these reconstructions, artefacts and nonspecific fluorescence are reconstructed. Artefacts can be due to areas that are slightly thicker at certain angles of view or to the mouse holder itself. The optical acquisition protocol has been adapted to suppress these views. Measurements with the industrial prototype confirm and extend that the proposed method can be used for *in vivo* imaging of tumors in mice. Increased protease activity was visualized in the tissue of subcutaneous tumor xenografts. Autofluorescence seems not to be an issue in this kind of experiments even if the mice are not on a chlorophyll-free diet prior to measuring. The systems were successfully applied to different regions of the mouse anatomy that is, trachea, abdomen, pelvis, and for deeply sited tumors/fluorophore inclusions as well as for subcutaneous tumors.

In this paper, the optical reconstructions were performed with no prior knowledge on the position of the fluorophore. The use of XCT as prior knowledge offers others advantages [26, 27]. It allows, for example, to speed up the computation by introducing some spatial constraints and prior knowledge [28]. Future work will address the use of *a priori* as a regularization factor in the optical reconstruction scheme and particularly in a better estimation of the "heterogeneities map" increasing the accuracy of the reconstructions of the parameters extracted from optical measurements more accurate. Furthermore, knowing the position of the organs from the CT reconstruction, and constraining the optical reconstruction algorithm, the optical reconstruction of the fluorescence would be also more accurate [29].

The precise coregistering of fDOT with X-ray μCT data/images allows evaluation of molecular information from marked labelled tissue within its anatomical context.

Acknowledgments

This paper was funded by a grant from SCANCO MEDICAL AG, Fabrikweg 2, 8306 Bruttisellen Switzerland. The animal model used at LETI is provided by Ralph Meuwissen, Centre Recherche INSERM U823 Equipe 2, Institut Albert Bonniot 38706 La Tronche Cedex, Grenoble, France. The animal model used at SCANCO is provided by group Markus Rudin, Inst Biomed. Engineering, UZH/ETHZ, Switzerland.

References

[1] V. Ntziachristos, E. A. Schellenberger, J. Ripoll et al., "Visualization of antitumor treatment by means of fluorescence molecular tomography with an annexin V-Cy5.5 conjugate," *Proceedings of the National Academy of Sciences of the United States of America*, vol. 101, no. 33, pp. 12294–12299, 2004.

[2] J. O. Deguchi, M. Aikawa, C. H. Tung et al., "Inflammation in atherosclerosis—visualizing matrix metalloproteinase action in macrophages *in vivo*," *Circulation*, vol. 114, no. 1, pp. 55–62, 2006.

[3] K. Licha and C. Olbrich, "Optical imaging in drug discovery and diagnostic applications," *Advanced Drug Delivery Reviews*, vol. 57, no. 8, pp. 1087–1108, 2005.

[4] L. Sancey, S. Dufort, V. Josserand et al., "Drug development in oncology assisted by noninvasive optical imaging," *International Journal of Pharmaceutics*, vol. 379, no. 2, pp. 309–316, 2009.

[5] A. Koenig, L. Hervé, G. Gonon et al., "Fluorescence diffuse optical tomography for free-space and multifluorophore studies," *Journal of Biomedical Optics*, vol. 15, no. 1, Article ID 016016, 2010.

[6] V. Ntziachristos, A. G. Yodh, M. D. Schnall, and B. Chance, "MRI-guided diffuse optical spectroscopy of malignant and benign breast lesions," *Neoplasia*, vol. 4, no. 4, pp. 347–354, 2002.

[7] F. Stuker, C. Baltes, K. Dikaiou et al., "Hybrid small animal imaging system combining magnetic resonance imaging with fluorescence tomography using single photon avalanche diode detectors," *IEEE Transactions on Medical Imaging*, vol. 30, no. 6, pp. 1265–1273, 2011.

[8] Q. Zhu, T. Durduran, V. Ntziachristos, M. Holboke, and A. G. Yodh, "Imager that combines near-infrared diffusive light and ultrasound," *Optics Letters*, vol. 24, no. 15, pp. 1050–1052, 1999.

[9] J. Boutet, L. Herve, M. Debourdeau et al., "Bimodal ultrasound and fluorescence approach for prostate cancer diagnosis," *Journal of Biomedical Optics*, vol. 14, no. 6, Article ID 064001, 2009.

[10] R. G. Blasberg, "*In vivo* molecular-genetic imaging: multimodality nuclear and optical combinations," *Nuclear Medicine and Biology*, vol. 30, no. 8, pp. 879–888, 2003.

[11] A. da Silva, T. Bordy, M. Debourdeau, J. M. Dinten, P. Peltié, and P. Rizo, "Coupling X-ray and optical tomography systems for *in vivo* examination of small animals," in *Proceedings of the 29th Annual International Conference of the IEEE Engineering in Medicine and Biology Society*, vol. 2007, pp. 3335–3338, Lyon, France, 2007.

[12] W. C. Barber, Y. Lin, O. Nalcioglu, J. S. Iwanczyk, N. E. Hartsough, and G. Gulsen, "Combined fluorescence and X-ray tomography for quantitative *in vivo* detection of fluorophore," *Technology in Cancer Research and Treatment*, vol. 9, no. 1, pp. 45–51, 2010.

[13] D. Kepshire, N. Mincu, M. Hutchins et al., "A microcomputed tomography guided fluorescence tomography system for small animal molecular imaging," *Review of Scientific Instruments*, vol. 80, no. 4, Article ID 043701, 2009.

[14] R. B. Schulz, A. Ale, A. Sarantopoulos et al., "Hybrid system for simultaneous fluorescence and X-ray computed tomography," *IEEE Transactions on Medical Imaging*, vol. 29, no. 2, pp. 465–473, 2010.

[15] N. Deliolanis, T. Lasser, D. Hyde, A. Soubret, J. Ripoll, and V. Ntziachristos, "Free-space fluorescence molecular tomography utilizing 360° geometry projections," *Optics Letters*, vol. 32, no. 4, pp. 382–384, 2007.

[16] A. Koenig, L. Hervé, J. Boutet et al., "Fluorescence diffuse optical tomographic system for arbitrary shaped small animals," in *Proceedings of the 5th IEEE International Symposium on Biomedical Imaging: From Nano to Macro, (ISBI '08)*, pp. 1593–1596, Paris, Farnce, 2008.

[17] A. Koenig, A. Planat-Chrétien, J. G. Coutard et al., "Development of a bi-modality XCT-DOT instrument," in *Progress in Biomedical Optics and Imaging (BIOS '10)*, F. S. Azar and X. Intes, Eds., vol. 7557 of *Proceedings of SPIE*, p. 755709, 2010, Edited by Azar, Fred S., Intes, Xavier.

[18] A. Koenig, L. Hervé, A. da Silva et al., "Whole body small animal examination with a diffuse optical tomography instrument," *Nuclear Instruments and Methods in Physics Research A*, vol. 571, no. 1-2, pp. 56–59, 2007.

[19] J. Boutet, A. Koenig, L. Hervé et al., "Optical tomograph optimized for tumor detection inside highly absorbent organs," *Optical Engineering*, vol. 50, no. 5, Article ID 053203, 2011.

[20] http://www.scanco.ch.

[21] I. A. Feldkamp, L. C. Davis, and J. W. Kress, "Practical cone-beam algorithm," *Journal of the Optical Society of America A*, vol. 1, no. 6, pp. 612–619, 1984.

[22] A. Planat-Chrétien, A. Koenig, J. G. Coutard, L. Hervé, M. Brambilla, and J. M. Dinten, "Toward absolute quantification in CW-FDOT systems: use of a priori information," in *European Conferences on Biomedical Optics and Imaging (ECBO '11)*, vol. 8088 of *Proceedings of SPIE*, Munich, Germany, May 2011.

[23] L. Hervé, A. Koenig, A. da Silva et al., "Noncontact fluorescence diffuse optical tomography of heterogeneous media," *Applied Optics*, vol. 46, no. 22, pp. 4896–4906, 2007.

[24] L. Hervé, A. Koenig, and J.-M. Dinten, "Non-uniqueness in fluorescence-enhanced continuous wave diffuse optical tomography," *Journal of Optics*, vol. 13, no. 1, Article ID 015702, 2011.

[25] R. C. Haskell, L. O. Svaasand, T. T. Tsay, T. C. Feng, M. S. McAdams, and B. J. Tromberg, "Boundary conditions for the diffusion equation in radiative transfer," *Journal of the Optical Society of America A*, vol. 11, no. 10, pp. 2727–2741, 1994.

[26] Y. Zhang, D. H. Brooks, and D. A. Boas, "A haemodynamic response function model in spatio-temporal diffuse optical tomography," *Physics in Medicine and Biology*, vol. 50, no. 19, pp. 4625–4644, 2005.

[27] M. J. Holboke, B. J. Tromberg, X. Li et al., "Three-dimensional diffuse optical mammography with ultrasound localization in a human subject," *Journal of Biomedical Optics*, vol. 5, no. 2, pp. 237–247, 2000.

[28] B. W. Pogue, T. O. McBride, J. Prewitt, U. L. Osterberg, and K. D. Paulsen, "Spatially variant regularization improves diffuse optical tomography," *Applied Optics*, vol. 38, no. 13, pp. 2950–2961, 1999.

[29] Y. Lin, H. Yan, O. Nalcioglu, and G. Gulsen, "Quantitative fluorescence tomography with functional and structural a priori information," *Applied Optics*, vol. 48, no. 7, pp. 1328–1336, 2009.